Journal of Materiomics xxx (xxxx) xxx

Contents lists available at ScienceDirect

Journal of Materiomics

journal homepage: www.journals.elsevier.com/journal-of-materiomics/

Research paper

Structural and microstructural description of relaxor-ferroelectric transition in quenched $Na_{1/2}Bi_{1/2}TiO_3$—$BaTiO_3$

Andreas Wohninsland [a, *], Ann-Katrin Fetzer [a], Rachel Broughton [b], Jacob L. Jones [b], K.V. Lalitha [a, **]

[a] Department of Materials- and Geosciences, Technical University of Darmstadt, 64287, Darmstadt, Germany
[b] Department of Materials Science and Engineering, North Carolina State University, Raleigh, NC, 27695, USA

ARTICLE INFO

Article history:
Received 20 October 2021
Received in revised form
5 January 2022
Accepted 22 January 2022
Available online xxx

Keywords:
Lead-free
Quenching
$Na_{1/2}Bi_{1/2}TiO_3$-$BaTiO_3$
Synchrotron diffraction
Ferroelectric

ABSTRACT

Quenching lead-free $Na_{1/2}Bi_{1/2}TiO_3$-based ceramics from sintering temperature is established to increase the depolarization temperature, T_d and the lattice distortion. *In situ* synchrotron X-ray diffraction measurements were carried out on furnace cooled and quenched $Na_{1/2}Bi_{1/2}TiO_3$ - $BaTiO_3$ (NBT-BT) with 6 and 9 mol. % BT to discern the field-induced ferroelectric order. Phase fractions were determined from full pattern Rietveld refinements and utilized together with the change in unit cell volume to calculate volumetric strain resulting from phase transformations. NBT-6BT demonstrates a cubic symmetry in the furnace cooled state but quenching stabilizes the rhombohedral *R*3*c* phase and delays the formation of a field-induced, long range-ordered tetragonal phase, thereby shifting the onset of macroscopic strain to higher fields. A field-induced phase transition from a weakly distorted rhombohedral to tetragonal phase can be observed in furnace cooled NBT-9BT. However, this phase transition cannot be detected in quenched NBT-9BT, since the ferroelectric tetragonal *P*4*mm* phase is stabilized in the initial state. In contrast to the furnace cooled materials, both the quenched compositions exhibit overall negligible volumetric strain as a function of electric field. Furthermore, scanning electron micrographs of chemically etched, poled and unpoled samples reveal an increased lamellar domain contrast in the quenched materials. All these findings strengthen the hypothesis of a stabilized ferroelectric order resulting in the absence of a field-induced phase transformation in quenched NBT-BT.

1. Introduction

In the past decades, the market of piezoelectrics has been dominated by lead-based materials. However, growing environmental concerns due to the toxicity of lead render it a necessity to find lead-free alternatives for widely used lead-based piezoelectric materials [1,2]. The relaxor ferroelectric $Na_{1/2}Bi_{1/2}TiO_3$ - $BaTiO_3$ (NBT-BT) system was first described in 1991 [3]. NBT-based materials exhibit great potential for high power applications [4–6]. Relaxor ferroelectrics differ from normal ferroelectrics by the presence of a strong frequency dispersion in the dielectric response. Their structure is simplistically described as a cubic matrix with non-cubic, polar, nanometer-sized inclusions labelled as polar nanoregions (PNRs) [7,8].

NBT-BT features a morphotropic phase boundary (MPB) located around a BT content of 5–10 mol. % [3,9,10] between the relaxor NBT and the ferroelectric, tetragonal BT end members. Even though NBT is often described as rhombohedral (*R*3*c*) [11], evidence exists for a much more complex crystal structure including lower symmetry space groups such as monoclinic (*Cc*) [12,13] and hierarchical structures [14,15]. The overall structural disorder of NBT is connected to the A-site disorder and off-centering of the Bi^{3+}-ion [16,17]. While NBT-BT is a tetragonal ferroelectric with a *P*4*mm* space group at a BT-content of >11 mol. %, the structure at the MPB is more complex. It is mainly described as a phase mixture of weakly distorted rhombohedral and tetragonal phases on the meso-to nanoscale [9,18] but as cubic-like on a global scale with very weak non-cubic distortions, if any [19,20]. Since the sensitivity of X-ray diffraction is not sufficient to detect such small distortions of the

* Corresponding author.()
** Corresponding author.()
E-mail addresses: wohninsland@ceramics.tu-darmstadt.de (A. Wohninsland), fetzer@geo.tu-darmstadt.de (A.-K. Fetzer), rabrough@ncsu.edu (R. Broughton), JacobJones@ncsu.edu (J.L. Jones), venkataraman@ceramics.tu-darmstadt.de (K.V. Lalitha).

Peer review under responsibility of The Chinese Ceramic Society.

https://doi.org/10.1016/j.jmat.2022.01.006

structure at the MPB, the material is commonly described as pseudo-cubic [20,21]. However, the aforementioned coexistence of rhombohedral and/or tetragonal phases on a meso-to nanoscopic scale was corroborated by different techniques, which allow probing of the local structure. Using Raman spectroscopy, Wylie-van Eerd *et al.* showed that MPB compositions of NBT-BT contain rhombohedral and tetragonal phases in the poled and unpoled state and even at temperatures above the depolarization temperature [22]. Electron diffraction patterns recorded via transmission electron microcopy (TEM) reveal superlattice reflections proving the coexistence of rhombohedral *R*3*c* and tetragonal *P*4*bm* symmetries at the MPB [18,23–25]. In single crystal NBT-4BT, rhombohedral nanoregions most likely separated by a tetragonal phase were reported based on diffuse X-ray scattering [26]. Using diffuse and quasielastic neutron-scattering, Pforr *et al.* described NBT-3.6BT as tetragonal platelets embedded in a rhombehedral matrix [27,28].

Furthermore, MPB compositions of NBT-BT are classified as nonergodic relaxors [29,30], whereby, the material undergoes an irreversible transition from relaxor to ferroelectric state upon application of an electric field or stress [31,32]. Heating the material above the ferroelectric to relaxor transition temperature, T_{F-R} transforms it back to the relaxor state. The application of NBT-BT is hindered by the material's low depolarization temperature, T_d which is dictated by T_{F-R} and coincides with the disappearance of the ferroelectric *P*4*mm* phase [33]. Therefore, several attempts have been made to improve the thermal stability by chemical modification [34–36], the formation of composites [6,37] and quenching the material rapidly from close to sintering temperature [38,39]. Quenching was shown to increase the T_d of NBT-BT by up to 60 °C depending on the composition [40,41] and to introduce changes in structure such as enhanced lattice distortion [38], increased off-centering of the A-site occupying Bi^{3+}-ion [42] and higher PNR volume fraction at elevated temperatures [41], apart from enhancing the conductivity [40,43,44]. These observations were used to hypothesize a stabilized ferroelectric order, leading to an increase in T_d [40]. This is especially noticeable for NBT-9BT, which spontaneously (without any external stimuli) transforms into a ferroelectric upon quenching [40].

In piezoelectric materials, structural properties under applied fields including lattice extension and phase transitions are directly linked with properties such as the converse piezoelectric coefficient [45,46]. Therefore, understanding field-induced phase transitions and other structural changes in a material system is critical to effectively tailor the material's properties. In the case of nonergodic relaxor NBT-BT, the field-induced transition from relaxor to ferroelectric state is accompanied by long-range ordered rhombohedral and tetragonal structures [21,47–49] and the aforementioned, average pseudo-cubic phase disappears [50].

Since quenching NBT-BT is hypothesized to stabilize a ferroelectric order (here we refer to the quenching-induced ferroelectric order that develops partially/wholly depending on composition to exhibit characteristics akin to that of poled NBT-BT [25]), it becomes pertinent to probe the field-induced phase transition in order to establish the relaxor/ferroelectric stability. To this end, quenched samples of NBT-BT with 6 and 9 mol. % BT are compared to furnace cooled specimen by utilizing *in situ* electric field-dependent synchrotron X-ray diffraction to investigate the phase transformation and calculate the resulting volumetric strain. The microstructural evidence is provided by scanning electron microscopy (SEM) of chemically-etched poled and unpoled samples.

2. Experimental section

NBT-BT ceramic powders with 6 and 9 mol. % BT substitution (abbreviated as e.g. NBT-6BT for 6 mol. % BT) were prepared via solid state synthesis route. Raw powders of Na_2CO_3 (99.5 %), $BaCO_3$ (99.8 %), Bi_2O_3 (99.975 %) and TiO_2 (99.6 %) (all Alfa Aesar, Thermo Fisher Scientific, Kandel, Germany) were dried at 100 °C for 24 h before weighing. Stoichiometric ratio of raw powders were milled in a planetary ball mill at 250 rpm for 24 h with zirconia balls and ethanol as milling medium. The resulting powders were dried and calcined at 900 °C for 3 h, followed by a second milling step. The calcined powders were sieved, pressed into pellets and sintered at 1150 °C for 3 h with a heating rate of 5 °C/min. Reference samples were cooled inside the furnace and are referred to as 'FC' (furnace cooled). Another set of samples were taken out of the furnace after the sintering dwell time of 3 h and rapidly cooled to room temperature assisted by a conventional air fan. These samples are referred to as 'Q' (quenched).

The surfaces of the ceramic discs were ground and silver electrodes were applied via sputtering. Rectangular bars of $1 \times 1 \times 6.7$ mm^3 were cut out and annealed at 400 °C for 30 min to relieve residual stresses. *In situ* synchrotron X-ray diffraction measurements were carried out at the 11-ID-C beamline (Advanced Photon Source, Argonne National Laboratory) in transmission geometry. An incident X-ray beam with a wavelength of 0.1173 Å (105.7 keV) and beam size of 0.5×0.5 mm^2 was used. 2D diffraction patterns were recorded with a PerkinElmer 2D detector at a physical detector distance of 2322 mm. Stepwise electric field was applied from 0 to 6 kV/mm with a step size of 0.5 kV/mm and 30 s holding time at each step to equilibrate before collecting a pattern. A diffraction pattern of a powder CeO_2 standard was recorded as reference.

The resulting 2D diffraction patterns were divided into 10 sectors with critical angles of 10° using DAWN software Version 2.15.0 [51]. The sector integrated from $\Psi = -5° - 5°$ is referred to as $\Psi = 0°$ and corresponds to scattering vectors most closely parallel to the electric field direction. Other vectors are referenced as Ψ from 10° to 90°. The measurement setup and subdivision in sectors was done like visualized in Ref. [52]. Full pattern refinements of the data obtained at $\Psi = 45°$ were carried out using TOPAS V6. To refine the instrumental parameters, the diffraction pattern of the CeO_2 standard was utilized. In addition to the full pattern refinements, peak fitting of selected reflections with pseudo-Voigt profile functions was used to evaluate the changes in unit cell volume as a function of electric field amplitude.

Longitudinal macroscopic strain measurements were carried out as a function of applied electric field using a Sawyer-Tower circuit and an optical displacement sensor. The incremental field steps were applied in the same way as during the *in situ* X-ray diffraction measurements to correlate with the calculated parameters from the diffraction patterns.

Disk-shaped pellets of all compositions were fabricated for microstructural investigations. These samples were polished with 15, 6, 3, 1 and ¼ μm diamond paste. Part of the samples were electroded with conductive silver lacquer and poled in a silicon oil bath at room temperature by application of an electric field of 6 kV/mm for 20 min. Subsequently, the electrodes were removed with acetone and chemical etching was performed by immersing the samples into a solution of 4% HCl, 2% HF and 94% distilled water for 30–60 s. The samples were carbon coated before the SEM images were recorded with a JEOL JSM 7600F (JEOL, Tokyo, Japan) in the backscattered electron (BSE) mode.

3. Results and discussion

3.1. Field-induced relaxor-to-ferroelectric transformation

The evolution of peak profiles as a function of electric field is depicted in Fig. 1 for two primary sets of reflections. To be consistent in referring to these sets of reflections across multiple phases, we

report the profile(s) relative to the cubic cell, or a pseudo-cubic (PC) reference frame. Fig. 1 shows the 111_{pc} and 200_{pc} profiles of NBT-6BT FC and NBT-6BT Q parallel to the direction of electric field ($\Psi = 0°$). Fig. 1a-d displays the evolution of these profiles with electric field as contour plots, while Fig. 1e-h contrasts the differences of the profiles before application of an electric field and at the maximum applied field. 111_{pc} and 200_{pc} are the critical profiles for observing rhombohedral (R) and tetragonal (T) distortions in the material, respectively. NBT-6BT FC appears as cubic in the zero-field state, most likely due to the limitations in the resolution of X-ray diffraction [20,32,40,48] (Fig. 1e and g). Between 1.5 and 2.0 kV/mm, peak splitting in 111_{pc} and 200_{pc} (Fig. 1a and b) sets in (marked by the dashed magenta line), accompanied by the appearance of a superlattice reflection (SR) (Fig. 1a). The SR is located at $2\theta \approx 2.86°$ and characteristic of the rhombohedral *R3c* phase or monoclinic *Cc* phase. However, evidence for the presence of *Cc* phase could not be observed in the limits of the diffraction resolution. Therefore, we conclude a field-induced phase transformation from average cubic (C) to R and T. It was reported in literature that this electric field-induced transformation can be observed at field amplitudes around 1.6 kV/mm with *in situ* X-ray diffraction experiments on NBT-7BT at room temperature [21] and around 2.3 kV/mm derived from thermometry data of NBT-6BT [53], which is in close agreement with the present study. Further increase in field amplitude causes a shift in relative peak intensities at ~5 kV/mm (dashed green line) in the 111_{pc} doublet, which hints towards a domain switching event.

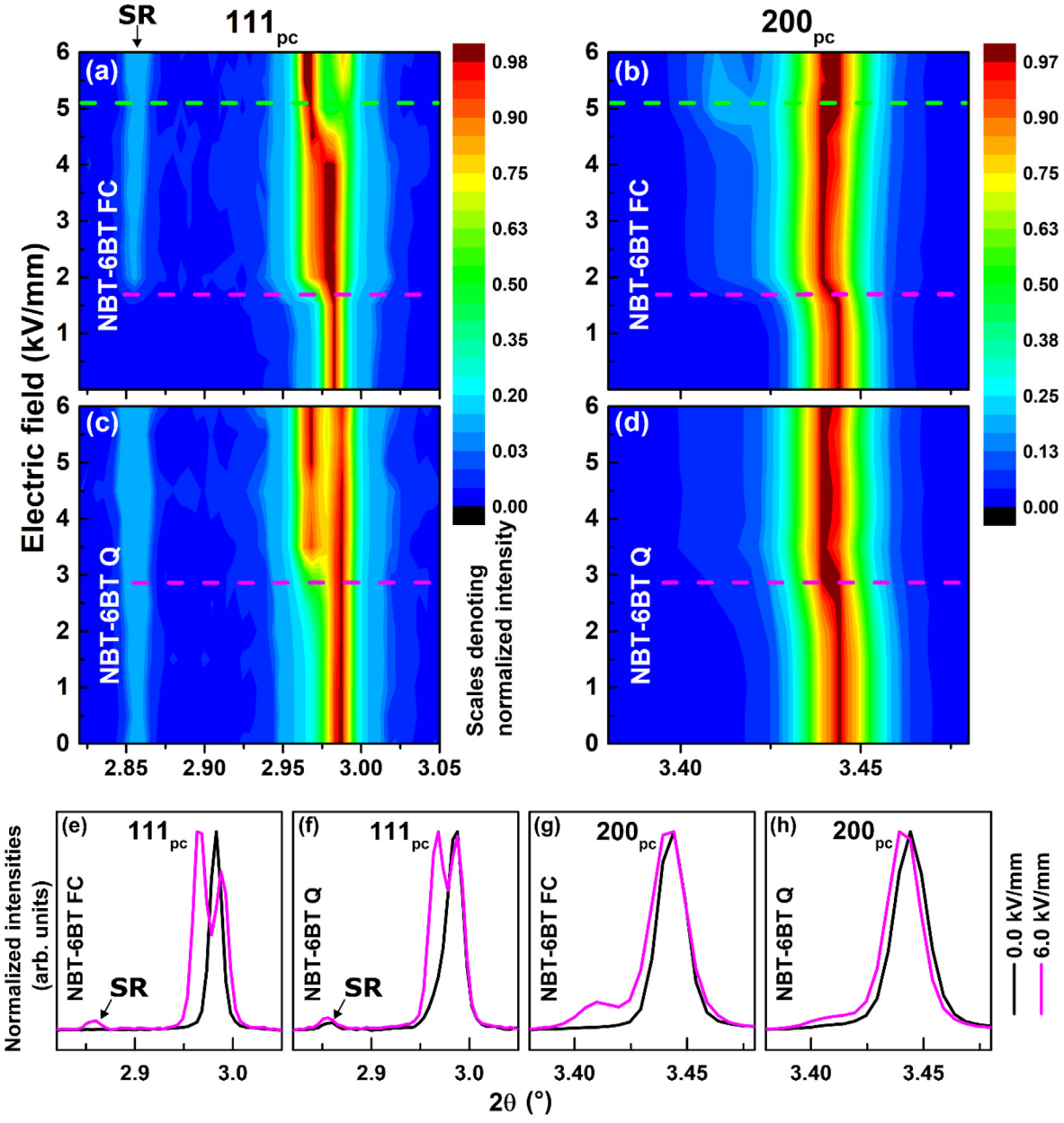

Fig. 1. *In situ* synchrotron X-ray diffraction patterns of NBT-6BT FC and NBT-6BT Q during application of electric field, starting from the unpoled state. (a) and (b) depict the evolution of the 111_{pc} and 200_{pc} profiles upon application of electric field ($\Psi = 0°$) from the unpoled state of NBT-6BT FC. (c) and (d) depict the same for NBT-6BT Q. Horizontal dashed lines indicate the appearance of new reflections (magenta) or prominent shift in intensity of existing reflections (green). (e)–(h) compares the hkl_{pc} reflections at zero and maximum field for $\Psi = 0°$. SR marks the superlattice reflection in (a), (c), (e) and (f).

NBT-6BT Q already features a splitting in the 111_{pc} profile accompanied by a SR in the initial state (Fig. 1c), while the 200_{pc} reflection is a singlet (Fig. 1h), substantiating the existence of R phase even before application of electric field [41]. This corroborates the stabilization of a long-range-ordered rhombohedral phase upon quenching. Between 2.5 and 3.0 kV/mm, the peak splitting in 111_{pc} becomes more prominent (Fig. 1b) and a weak splitting in 200_{pc} starts to appear (Fig. 1d), both marked by the dashed magenta line, indicating a phase transformation.

The evolution of peak profile as a function of electric field is depicted as contour plots in Fig. 2a-d for the 111_{pc} and 200_{pc} profiles of NBT-9BT FC and NBT-9BT Q parallel to the direction of electric field ($\Psi = 0°$). Fig. 2e-h contrasts the differences of the critical reflections before application of electric field and at the maximum applied field. Before application of electric field, NBT-9BT FC features a singlet in 111_{pc} (Fig. 2e), while the 200_{pc} profile shows a weak splitting (Fig. 2g) which is associated with the existence of tetragonal distortions [9]. In tetragonal materials, the 200 reflection of the cubic phase splits into two reflections, namely 002_T at lower 2θ angles and 200_T at higher 2θ angles, respectively. Between 0.5 and 1.0 kV/mm (Fig. 2b, magenta dashed line), the intensity of the 002_T reflection increases strongly, indicating a phase transformation.

For both NBT-9BT FC and NBT-9BT Q, no splitting of the 111_{pc} profile is observed - neither in the initial state nor under application of an electric field (Fig. 2a, c, e and f). The 200_{pc} profile of NBT-

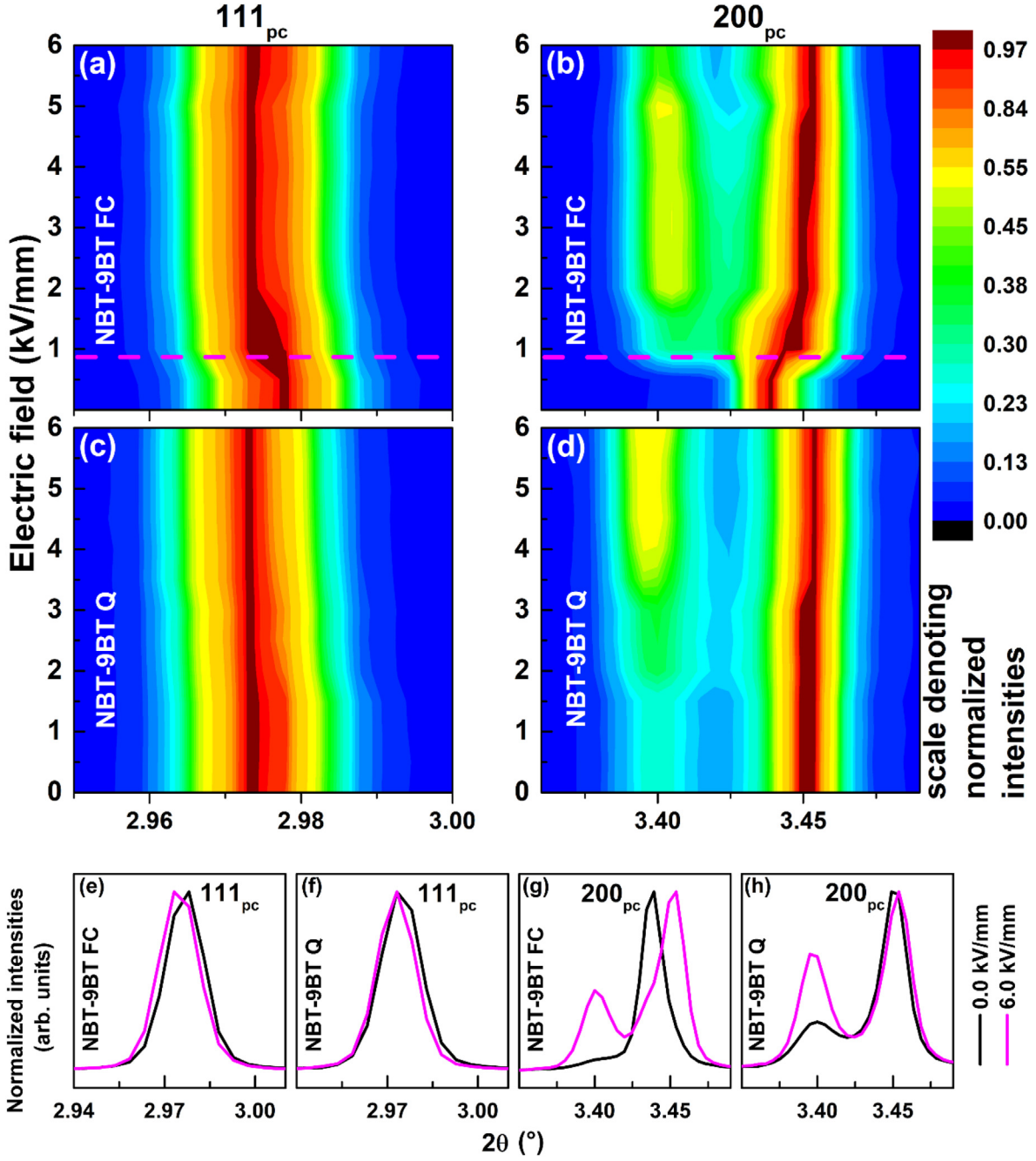

Fig. 2. *In situ* synchrotron X-ray diffraction patterns of NBT-9BT FC and NBT-9BT Q during application of electric field, starting from the unpoled state. (a) and (b) depict the evolution of the 111_{pc} and 200_{pc} reflections upon application of electric field ($\Psi = 0°$) from the unpoled state of NBT-9BT FC. (c) and (d) depict the same for NBT-9BT Q. The horizontal dashed line indicates a phase transformation. (e)–(h) compares the hkl_{pc} reflections at zero and maximum field with $\Psi = 0°$.

9BT Q already shows a clear splitting in the initial state (Fig. 2h), which is stronger than that of NBT-9BT FC. Upon application of an electric field, no abrupt change in peak intensities or peak position is observed. The only visible effect is a gradual shift of peak intensities in the doublet within the 200_{pc} profile (Fig. 2d). This absence of field-induced changes (in contrast to NBT-6BT FC and NBT-6BT Q) correlates with the findings of K. V. Lalitha *et al.* [40], wherein a spontaneous ferroelectric order upon quenching NBT-9BT was established from dielectric data, accompanied by an increase in lattice distortion. A spontaneous ferroelectric order was also previously evidenced in NBT-9BT composites with ZnO inclusions, which also demonstrated increase in T_d, akin to NBT-9BT Q [54]. Note the slight shift of the 111_{pc} profile of both NBT-9BT FC and NBT-9BT Q towards lower 2θ values, indicating an extension of the unit cell in direction of the electric field (Fig. 2e and f).

As reported earlier, at higher electric fields, all the investigated compositions are in a ferroelectric state [40]. Electric field-induced crystallographic texturing in a ferroelectric material is directly associated with the fraction of realigned domains. Texture factors (f), which reflect pole densities in units of multiples of a random distribution (MRD), were calculated to compare domain switching of FC and Q samples. Fig. 3a-d shows the 111_{pc} reflections for NBT-6BT FC and NBT-6BT Q and the 200_{pc} reflection for NBT-9BT FC and NBT-9BT Q at maximum applied fields of 6 kV/mm for different angles with respect to the electric field (Ψ). Texturing is clearly visible in all the materials, apparent from the change in peak intensities as a function of Ψ. Texture factor for the dominant phase of each composition was calculated at maximum field using the 45° data as reference state with the following equations [47,55,56].

$$f_{111} = 4\frac{\frac{I_{111}}{I'_{111}}}{\frac{I_{111}}{I'_{111}} + 3\,\frac{I_{11\bar{1}}}{I'_{11\bar{1}}}} \quad (1)$$

and

$$f_{002} = 3\frac{\frac{I_{002}}{I'_{002}}}{\frac{I_{002}}{I'_{002}} + 2\,\frac{I_{200}}{I'_{200}}} \quad (2)$$

where, I_{hkl} is the integrated *hkl* peak intensity at the respective angle and I'_{hkl} is the reference intensity at 45°. The Ψ = 45° sector, meaning the data integrated in the range Ψ = 40–50° was defined as the reference state for calculating the texture factors based on the shift in d-spacing of 200_{pc} single reflections and in accordance with literature [52]. In our case, the zero field state cannot serve as reference state due to the field-induced phase transition accompanied by peak splitting.

f_{111} values for NBT-6BT FC and NBT-6BT Q show close to no difference (at Ψ = 0° values of 2.00 and 2.07 MRD, respectively) at 6 kV/mm, meaning that quenching NBT-6BT does not affect the degree of texturing of the rhombohedral phase upon application of an electric field. Nevertheless, there is a significant difference between the texture strength of NBT-9BT FC and NBT-9BT Q. The tetragonal phase in NBT-9BT Q (1.35 MRD) exhibits stronger texture compared to NBT-9BT FC (1.23 MRD), with maximum values for f_{002} parallel to the direction of electric field (Ψ = 0°). An increase in texture factor for quenched samples indicates an increased domain switching fraction in the T phase upon application of electric field. One way to rationalize this are the different conditions of formation of the T phase in NBT-9BT FC and NBT-9BT Q. In NBT-9BT FC, the T phase is mainly electric field-induced and therefore, might not be strongly textured, as opposed to NBT-9BT Q, wherein, the T phase is for the most part already present in the initial state and hence, more susceptible to field-induced texturing.

Defining a nominally untextured reference state allows full pattern refinements to be carried out without having to use a texture model. Introducing a spherical harmonics model to account for texturing was attempted similar to what is reported in Ref. [57].

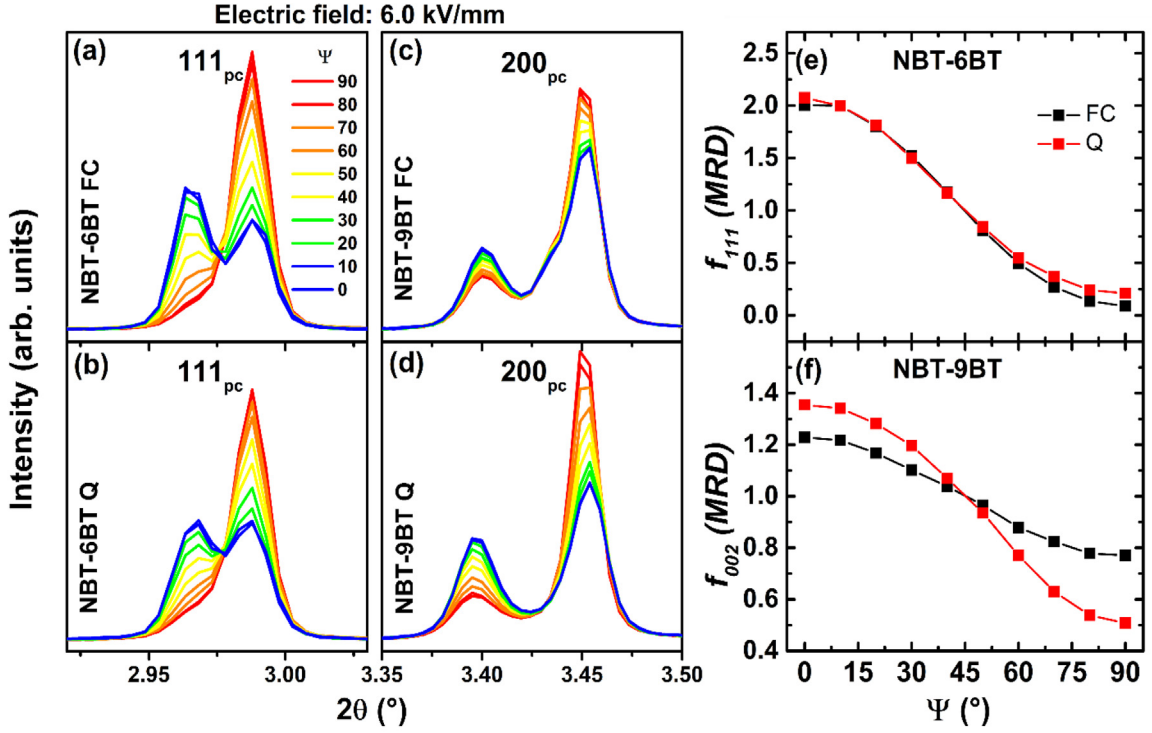

Fig. 3. 111_{pc} profile of NBT-6BT FC (a) and NBT-6BT Q (b) and 200_{pc} profile of NBT-9BT FC (c) and NBT-9BT Q (d) for different azimuthal ranges at 6.0 kV/mm. Calculated texture factors adopting the peak fitting approach for the rhombohedral phase of NBT-6BT FC and NBT-6BT Q (e) and the tetragonal phase of NBT-9BT FC and NBT-9BT Q (f).

A similar approach was successfully used on comparable data by Hinterstein *et al.* [48,58]. However, in our case the fits were unstable and did not converge to a reasonable minimum, most likely due to a larger number of refinement variables and a limited number of reflections to fit. Therefore, the approach of refining a nominally untextured state (random texture) without utilizing a texture model was adopted.

Fig. 4 shows the nominally untextured data at $\Psi = 45^\circ$ for all investigated materials. The FC data of both compositions (Fig. 4a and c) features much stronger changes in peak intensities, width and position compared to the Q data (Fig. 4b and d) with increasing electric field. Under the nominally untextured assumptions, changes in the diffraction profiles can only be attributed to a change in lattice parameters and/or phase transformations, but not to domain reorientation. Using the whole diffraction patterns at $\Psi = 45^\circ$, full pattern Rietveld refinements were carried out to evaluate the phase fraction and unit cell parameters. The absolute phase fraction established using this strategy does not account for the grain-scale strain heterogeneity noted for NBT-BT materials, wherein orientation-dependent phase evolution has been noted [59]. We rather adopt a comparative study using diffraction patterns at $\Psi = 45^\circ$ to track the influence of quenching-induced ferroelectric state on the field-induced relaxor-ferroelectric transformation.

Phase fraction for cubic, rhombohedral and tetragonal phases established via Rietveld refinements are presented in Fig. 5. NBT-6BT FC (Fig. 5a) is cubic in the initial state within the resolution limit of X-ray diffraction and was refined using a $Pm\bar{3}m$ phase model [20,48]. Between 1.5 and 2.0 kV/mm, NBT-6BT FC transforms from a single-phase cubic state into a two-phase mixture between dominant rhombohedral *R*3*c* (77%) and tetragonal *P*4*mm* phase (23%) [20,21,48]. Upon further increase of the electric field, the phase fractions evolve to 81% R and 19 % T phase at the maximum field amplitude of 6.0 kV/mm.

NBT-6BT Q (Fig. 5b) is a phase mixture already in the initial state fitted with 71% *R*3*c* and 29% $Pm\bar{3}m$. The quenching-induced lowering of the average symmetry caused by an increase in unit cell distortion was reported previously [25,38,41] and can be rationalized by a more pronounced off-centering of the Bi^{3+}-ion [42]. This leads to a globally more distorted structure, which can be resolved using XRD and manifests in our case in the evolution of average rhombohedral *R*3*c* symmetry. Upon application of electric field, the rhombohedral phase fraction in NBT-6BT Q increases to 80% *R*3*c* at 2.5 kV/mm, before transforming into a two phase system consisting of *R*3*c* and *P*4*mm* phases between 2.5 and 3.0 kV/mm. Upon further increasing the electric field, at first, the R phase content increases to 93% followed by a slight decrease to 88% at 6.0 kV/mm.

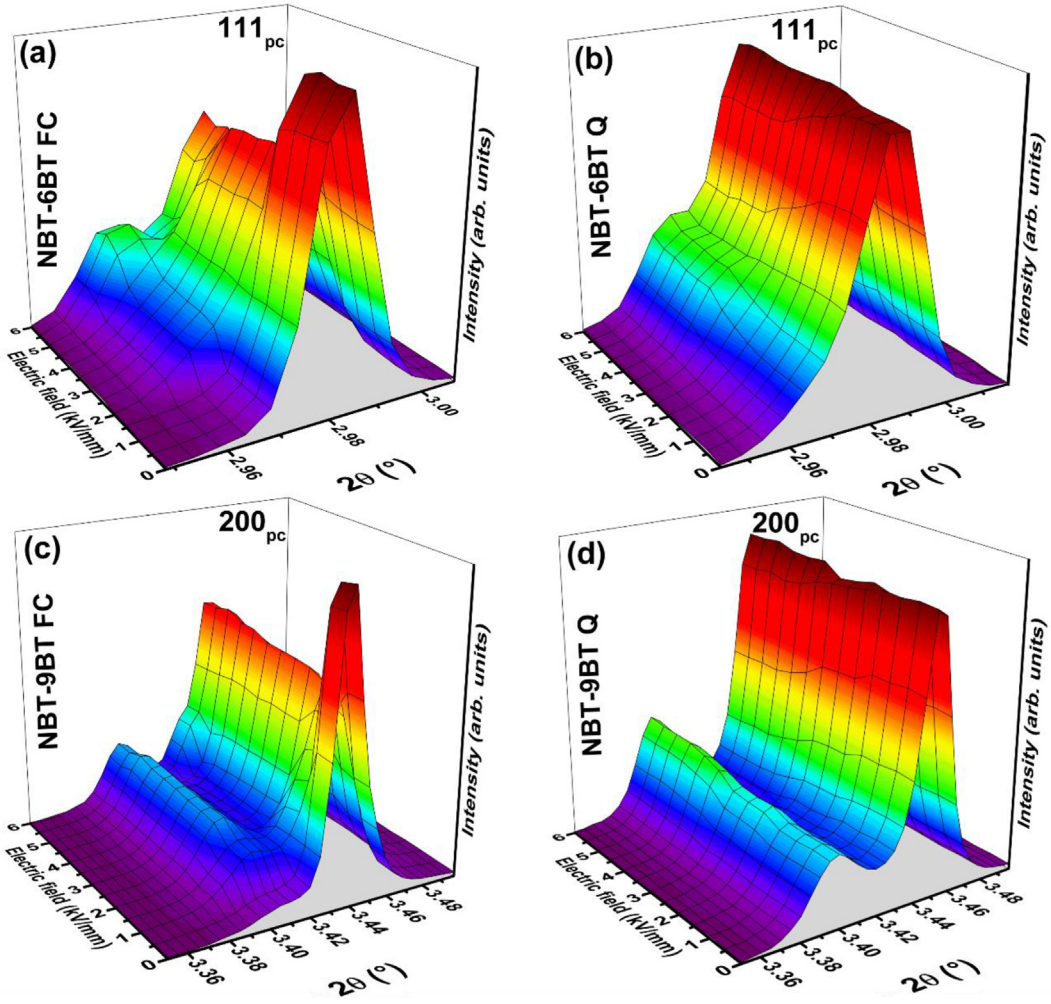

Fig. 4. 111_{pc} profiles of NBT-6BT FC and NBT-6BT Q (a and b) and 200_{pc} profiles of NBT-9BT FC and NBT-9BT Q (c and d) as a function of electric field. All the plots depict the diffraction data recorded at $\Psi = 45^\circ$.

NBT-9BT FC (Fig. 5c) exhibits an initial phase composition of 60% R and 40% T phase fitted with the space groups *R*3*m* and *P*4*mm*, respectively. A purely tetragonal phase model did not give a satisfactory fit. Note that, NBT-9BT FC does not show a splitting of the 111_{pc} reflection because of a very small rhombohedral distortion (Fig. 2e). However, a rhombohedral phase was used in accordance with literature, partly based on TEM findings [25,54]. At an electric field amplitude of 1.0 kV/mm, the *P*4*mm* phase fraction increases to 83% while the *R*3*m* phase fraction decreases to 17%. With further increasing field, the tetragonal phase fraction reaches a maximum at 5.0 kV/mm with 91% followed by a decrease to 82% at maximum field.

NBT-9BT Q was also refined using a two-phase mixture of *R*3*m* and *P*4*mm*, but with a significantly higher tetragonal phase fraction of 84% in the initial state compared to NBT-9BT FC. Upon application of electric field, the phase fractions do not change much. The tetragonal phase fraction increases to 89% at maximum field amplitude. This quantifies the absence of a phase transformation as indicated before by the peak profile evolution depicted in Fig. 2d and corroborates the stabilization of a ferroelectric order upon quenching [40]. None of the NBT-9BT compositions show a SR around $2\theta = 2.86°$. Therefore, the presence of *R*3*c* phase was excluded. Overall, the quenching-induced stabilization of ferroelectric order results only in dominant domain switching processes, as opposed to the furnace cooled specimen which undergoes relaxor-ferroelectric transformation, in accordance with prior studies [40,41].

3.2. Volumetric strain resulting from phase transformation

Evaluation of the phase fraction and change in unit cell volume as a function of electric field allows calculation of volumetric or phase transformation strain, ε^V, resulting from phase transformation using [21,60].

$$\varepsilon^V = \frac{1}{3}\left[\left(V_{field} - V_{initial}\right) \Big/ V_{initial}\right] \tag{3}$$

where, V_{field} and $V_{initial}$ are the average unit cell volumes at a certain field step or before application of an electric field, respectively. V is calculated as the weighted sum of the unit cell volume of the coexisting phases. Therefore, Eq (3), exemplarily for NBT-6BT FC after the phase transition, can be specified to

$$\varepsilon^V = \frac{1}{3}\left[\{(PF_R \times V_R) + (PF_T \times V_T) - V_C\} / V_C\right] \tag{4}$$

where, PF is the phase fraction of the respective phase and V_R, V_T and V_C are the unit cell volume of rhombohedral and tetragonal phase at a certain field and of the initial cubic phase, respectively. The unit cell volume is calculated using the lattice parameters of the respective phase averaged throughout the whole orientation space, e.g. for the rhombohedral lattice parameter [60].

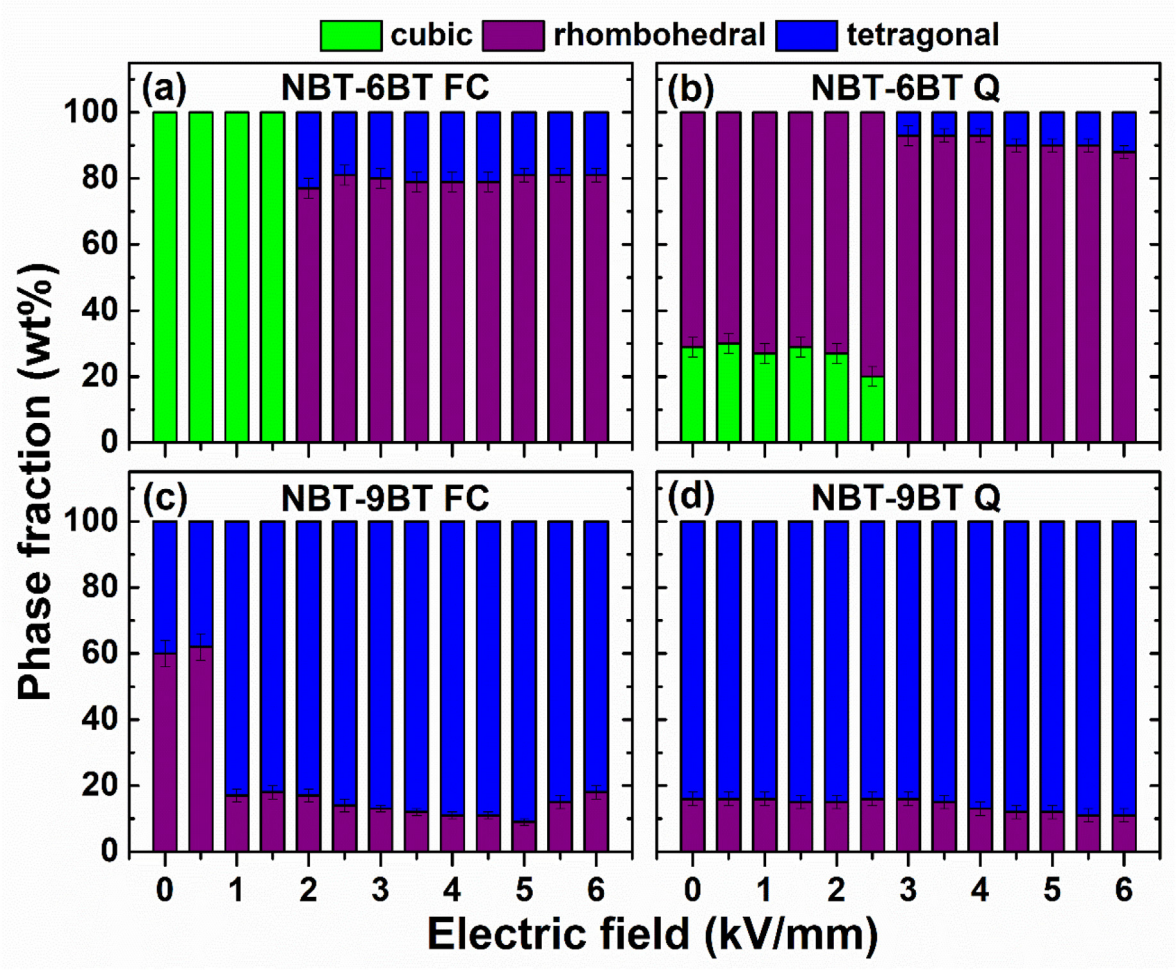

Fig. 5. Phase fraction as a function of electric field obtained using Rietveld refinement.

$$a_R = \int_{\propto=0}^{2\pi} a(\propto)\sin(\propto)d\propto \quad (5)$$

or in discrete form

$$a_R = \sum_{\propto=0^\circ}^{90^\circ} a(\propto)\left[\cos(\propto_i) - \cos(\propto_j)\right] \quad (6)$$

with $\propto_i$ and $\propto_j$ being the low and high boundaries of the respective azimuthal range. Fig. 6 depicts the calculated volumetric strains plotted together with macroscopic strain measured with the same stepwise increase of electric field and the same time at each field as in the *in situ* diffraction experiments. The macroscopic strain measurements reveal an increase in the switching field (inflection point of the strain curve) by 0.5 and 1.0−1.5 kV/mm for NBT-6BT and NBT-9BT upon quenching, respectively. The maximum strain is higher for NBT-6BT Q compared to NBT-6BT FC (0.47 and 0.42% respectively), while it is slightly lower for NBT-9BT Q compared to NBT-9BT FC (0.30 and 0.31% respectively), therefore, showing no consistent trend.

NBT-6BT FC and NBT-9BT FC (Fig. 6a and c) both show an increase in ε^V to ~ 0.12% at 2.0 kV/mm and ~ 0.07% at 1.0 kV/mm, respectively caused by the relaxor-to-ferroelectric transformation. This is followed by rather constant strain values with increasing field. Note that for both NBT-6BT FC and NBT-9BT FC, the inflection in the calculated strain occurs at the same field step at which the phase transformation sets in (Fig. 5a and c). When comparing ε^V of NBT-9BT FC with the macroscopic strain measurement, there is a 0.5 kV/mm difference in the inflection point of the strain response (Fig. 6c), which could be rationalized due to the differences in the experimental condition between the synchrotron measurement (sample exposed to a high energy X-ray beam) and the strain response obtained in the laboratory using a Sawyer-Tower circuit.

While both NBT-6BT FC and NBT-9BT FC show a correlation between the onset of macroscopic strain and ε^V, the Q compositions (Fig. 6b and d) do not exhibit a sudden increase in ε^V, even though a comparable increase in macroscopic strain can be observed regardless of FC or Q. Both NBT-6BT Q and NBT-9BT Q exhibit overall low values for ε^V. Even though NBT-6BT Q features a phase transformation, the quenched material does not exhibit an inflection in the volumetric strain. The absence of phase transition in NBT-9BT Q clearly reflects in ε^V values close to zero regardless of the applied field amplitude.

The quenching-induced ferroelectric order alters the phase transformation, resulting in overall negligible ε^V values in the case of both NBT-6BT Q and NBT-9BT Q. This absence of field-induced volumetric strain upon quenching correlates to what is known from prior works [40,41]. The absence/weakened structural changes upon application of an electric field in quenched NBT-BT evidenced in this diffraction study can be rationalized by the more pronounced off-centering of the Bi^{3+}-ion accompanied by an overall strong lattice distortion in quenched samples [42] in comparison to the furnace cooled samples [16,25]. Furthermore, quenching alters the equilibrium oxygen vacancy concentration due to freezing-in of the defect distribution from a high temperature state, reflecting as increased conductivity [40,44]. Both, the stronger Bi^{3+}-ion off-centering and the non-equilibrated oxygen vacancy concentration could lead to a consolidation of the structure promoting the spontaneous formation of a ferroelectric order without the need of an external stimulus [40]. This might ultimately lead to lower electric field-induced strain and delayed onset/absence of phase transformation in quenched NBT-BT (Fig. 6).

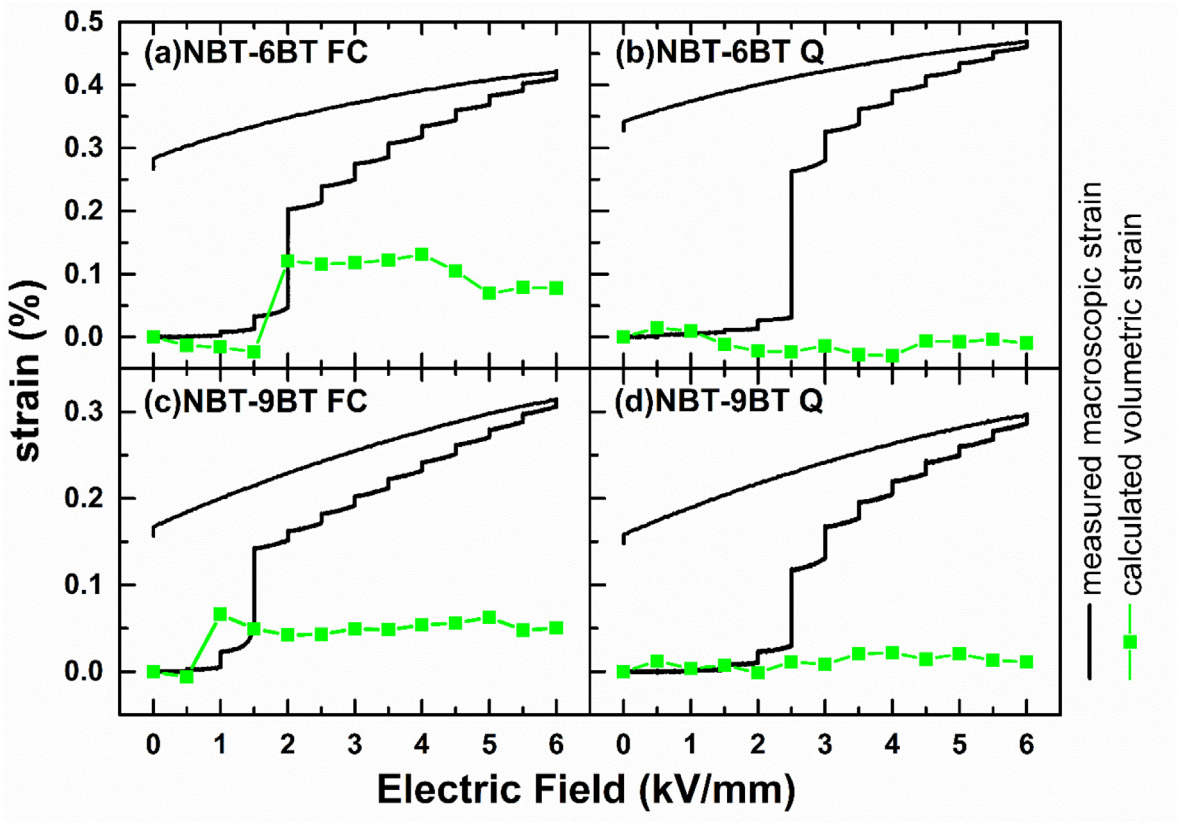

Fig. 6. Measured macroscopic strains and calculated volumetric strain ε^V as a function of electric field.

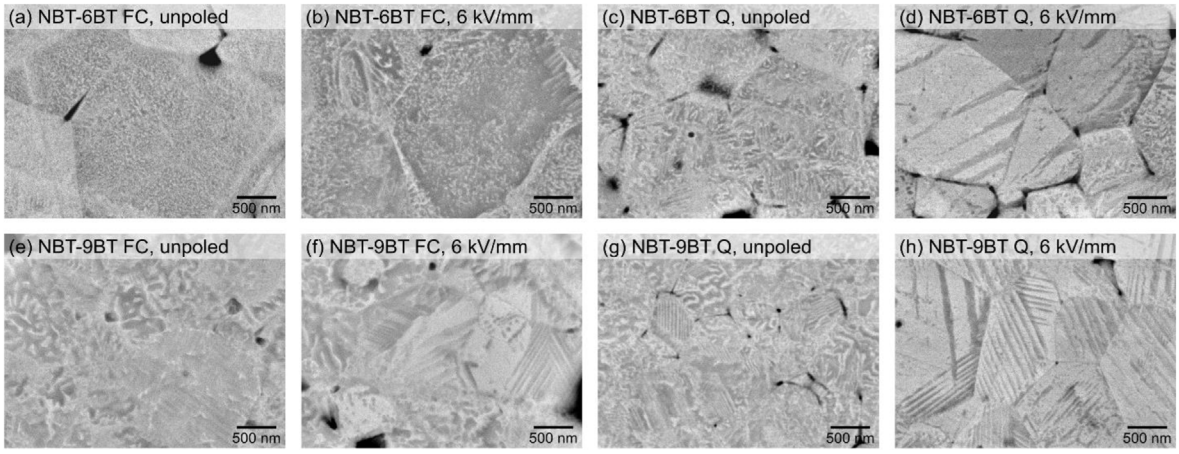

Fig. 7. SEM micrographs (BSE, 15 kV) of chemically etched unpoled and poled (6 kV/mm) NBT-6BT FC (a,b), NBT-6BT Q (c,d), NBT-9BT FC (e,f) and NBT-9BT Q (g,h).

Additionally, Das Adhikary and co-authors [33] correlated the depolarization of NBT-BT with ≥6 mol.% BT with the disappearance of ferroelectric *P*4*mm* phase. Since quenching stabilizes ferroelectric *P*4*mm* phase, as clearly evident from the results of NBT-9BT Q from this study, this stabilization can be assumed to hold also true at elevated temperatures, subsequently leading to an increase in the depolarization temperature as reported earlier [38,40,41].

3.3. Microstructural characterization: domain contrast

Differences in the domain structure are apparent in the SEM micrographs, featuring a trend towards an increased lamellar domain contrast for quenched and poled samples. In unpoled NBT-6BT FC (Fig. 7a), no long-range ordered domain structures appear, which is consistent with the relaxor state characterized by PNRs and the absence of lamellar domains. The equivalent poled sample (Fig. 7b) has a similar appearance in SEM, where domains are widely absent. Only very few local regions feature irregular domain contrast. In contrast, NBT-6BT Q already shows fine lamellar domains in the unpoled state (Fig. 7c). Such a morphology in NBT-BT hints towards the presence of tetragonal, ferroelectric domains [61]. The occurrence of lamellar domains corroborates a stabilized ferroelectric order upon quenching, also in accordance with the aforementioned literature [25], where an increased lamellar domain contrast was observed in NBT-6BT Q using TEM. After poling, the domains appear more prominent and have increased in width and length (Fig. 7d). NBT-9BT FC, which is located more on the tetragonal side of the MPB region, shows weak lamellar domains in the unpoled state (Fig. 7e). Upon poling, domains appear more abundant and pronounced (Fig. 7f). The same holds true for the NBT-9BT Q composition, however, the domains in the unpoled sample (Fig. 7g) appear more distinct compared to the FC state. A prominent domain contrast develops in NBT-9BT Q upon poling (Fig. 7h). This correlates with the slightly higher tetragonal phase fraction for NBT-9BT Q (89%) in comparison to NBT-9BT FC (82%) at maximum field (Fig. 5).

4. Conclusions

In this work, quenched and furnace cooled NBT-6BT and NBT-9BT ceramics were studied using *in situ* synchrotron electric field-dependent X-ray diffraction and scanning electron microscopy. Full pattern Rietveld refinements reveal an increase in rhombohedral phase fraction in quenched NBT-6BT, while in quenched NBT-9BT, the absence of a relaxor-to-ferroelectric transformation, accompanied by the stabilization of tetragonal ferroelectric phase is evidenced. This quenching-induced ferroelectric order results in strong reduction of volumetric strain upon application of electric field. The calculated volumetric strain is negligible/zero for the quenched materials, corroborating the delayed onset/absence of relaxor-to-ferroelectric transformation, depending on BT content. Additionally, SEM micrographs of chemically etched samples exhibit strong lamellar domain contrast for quenched samples even before poling, further validating the quenching-induced stabilization of ferroelectric order.

Declaration of competing interest

The authors declare that they have no known competing financial interests or personal relationships that could have appeared to influence the work reported in this paper.

Acknowledgements

This research used resources of the Advanced Photon Source, a U.S. Department of Energy (DOE) Office of Science User Facility, operated for the DOE Office of Science by Argonne National Laboratory under Contract No. DE-AC02-06CH11357. JJ and RB acknowledge support from the National Science Foundation (DMR-2004455). LKV, AKF and AW thank the Deutsche Forschungsgemeinschaft (DFG) for financial support under Nos. KO 5948/1-1 and KL 615/34-1 (Grant No. 414311761). The authors thank Maximilian Gehringer and Till Frömling for assistance with the experiment at the Advanced Photon Source.

References

[1] Bell AJ, Deubzer O. MRS Bull 2018;43:581–7. https://doi.org/10.1557/mrs.2018.154.
[2] Rödel J, Li J-F. MRS Bull 2018;43:576–80. https://doi.org/10.1557/mrs.2018.181.
[3] Takenaka T, Maruyama K, Sakata K. Jpn J Appl Phys 1991;1(30):2236–9. https://doi.org/10.1143/Jjap.30.2236.
[4] Tou T, Hamaguti Y, Maida Y, Yamamori H, Takahashi K, Terashima Y. Jpn J Appl Phys 2009;48:07gm03. https://doi.org/10.1143/Jjap.48.07gm03.
[5] Shibata K, Wang R, Tou T, Koruza J. MRS Bull 2018;43:612–6. https://doi.org/10.1557/mrs.2018.180.
[6] Slabki M, Lalitha KV, Rojac T, Rodel J, Koruza J. J Appl Phys 2021;130:014101. https://doi.org/10.1063/5.0052293.
[7] Polinger V, Bersuker IB. Phys Rev B 2018;98:214102. https://doi.org/10.1103/PhysRevB.98.214102.
[8] Bokov AA, Ye Z-G. J Adv Dielectr 2012;2:1241010. https://doi.org/10.1142/s2010135x1241010x.
[9] Ma C, Tan X. J Am Ceram Soc 2011;94:4040–4. https://doi.org/10.1111/j.1551-

2916.2011.04670.x.
[10] Jo W, Schaab S, Sapper E, Schmitt LA, Kleebe HJ, Bell AJ, et al. J Appl Phys 2011;110:074106. https://doi.org/10.1063/1.3645054.
[11] Smolenskii GA, Isupov VA, Agranovskaya AI, Krainik NN. 4. Sov Phys Solid State 1961;2:2651–4.
[12] Gorfman S, Thomas PA. J Appl Crystallogr 2010;43:1409–14. https://doi.org/10.1107/S002188981003342x.
[13] Aksel E, Forrester JS, Jones JL, Thomas PA, Page K, Suchomel MR. Appl Phys Lett 2011;98:152901. https://doi.org/10.1063/1.3573826.
[14] Levin I, Reaney IM. Adv Funct Mater 2012;22:3445–52. https://doi.org/10.1002/adfm.201200282.
[15] Dorcet V, Trolliard G. Acta Mater 2008;56:1753–61. https://doi.org/10.1016/j.actamat.2007.12.027.
[16] Aksel E, Forrester JS, Nino JC, Page K, Shoemaker DP, Jones JL. Phys Rev B 2013;87:104113. https://doi.org/10.1103/PhysRevB.87.104113.
[17] Paterson AR, Nagata H, Tan XL, Daniels JE, Hinterstein M, Ranjan R, et al. MRS Bull 2018;43:600–6. https://doi.org/10.1557/mrs.2018.156.
[18] Yao JJ, Monsegue N, Murayama M, Leng WN, Reynolds WT, Zhang QH, et al. Appl Phys Lett 2012;100:12901. https://doi.org/10.1063/1.3673832.
[19] Datta K, Neder RB, Richter A, Gobbels M, Neuefeind JC, Mihailova B. Phys Rev B 2018;97:184101. https://doi.org/10.1103/PhysRevB.97.184101.
[20] Garg R, Rao BN, Senyshyn A, Krishna PSR, Ranjan R. Phys Rev B 2013;88:14103. https://doi.org/10.1103/PhysRevB.88.014103.
[21] Khansur NH, Hinterstein M, Wang ZY, Groh C, Jo W, Daniels JE. Appl Phys Lett 2015;107:242902. https://doi.org/10.1063/1.4937470.
[22] Wylie-van Eerd B, Damjanovic D, Klein N, Setter N, Trodahl J. Phys Rev B 2010;82:104112. https://doi.org/10.1103/PhysRevB.82.104112.
[23] Ma C, Tan X, Dul'kin E, Roth M. J Appl Phys 2010;108:104105. https://doi.org/10.1063/1.3514093.
[24] Craciun F, Galassi C, Birjega R. J Appl Phys 2012;112:124106. https://doi.org/10.1063/1.4770326.
[25] Fetzer A-K, Wohninsland A, Hofmann K, Clemens O, Lalitha KV, Kleebe H-J. Open Ceramics 2021;5:100077. https://doi.org/10.1016/j.oceram.2021.100077.
[26] Daniels JE, Jo W, Rodel J, Rytz D, Donner W. Appl Phys Lett 2011;98:3966–74. https://doi.org/10.1063/1.3602316.
[27] Pforr F, Meyer KC, Major M, Albe K, Donner W, Stuhr U, et al. Phys Rev B 2017;96:184107. https://doi.org/10.1103/PhysRevB.96.184107.
[28] Pforr F, Major M, Donner W, Stuhr U, Roessli B. Phys Rev B 2016;94:014105. https://doi.org/10.1103/PhysRevB.94.014105.
[29] Ranjan R, Dviwedi A. Solid State Commun 2005;135:394–9. https://doi.org/10.1016/j.ssc.2005.03.053.
[30] Ranjan R. Curr Sci 2020;118:1507–19. https://doi.org/10.18520/cs/v118/i10/1507-1519.
[31] Schader FH, Wang ZY, Hinterstein M, Daniels JE, Webber KG. Phys Rev B 2016;93:134111. https://doi.org/10.1103/PhysRevB.93.134111.
[32] Jo W, Daniels JE, Jones JL, Tan X, Thomas PA, Damjanovic D, et al. J Appl Phys 2011;109:14110. https://doi.org/10.1063/1.3530737.
[33] Das Adhikary G, Mahale B, Rao BN, Senyshyn A, Ranjan R. Phys Rev B 2021;103:184106. https://doi.org/10.1103/PhysRevB.103.184106.
[34] Davies M, Aksel E, Jones JL. J Am Ceram Soc 2011;94:1314–6. https://doi.org/10.1111/j.1551-2916.2011.04441.x.
[35] Li L, Zhu MK, Zhou KL, Wei QM, Zheng MP, Hou YD. J Appl Phys 2017;122:204104. https://doi.org/10.1063/1.5012889.
[36] Lalitha KV, Zhu T, Salazar MP, Hofmann K, Waidha AI, Jaud JC, et al. J Am Ceram Soc 2020;104:2202–12. https://doi.org/10.1111/jace.17581.
[37] Riemer LM, Lalitha KV, Jiang XJ, Liu N, Dietz C, Stark RW, et al. Acta Mater 2017;136:271–80. https://doi.org/10.1016/j.actamat.2017.07.008.
[38] Muramatsu H, Nagata H, Takenaka T. Jpn J Appl Phys 2016;55:10tb07. https://doi.org/10.7567/Jjap.55.10tb07.
[39] Miura T, Nagata H, Takenaka T. Jpn J Appl Phys 2017;56:10pd05. https://doi.org/10.7567/Jjap.56.10pd05.
[40] Lalitha KV, Koruza J, Rodel J. Appl Phys Lett 2018;113:252902. https://doi.org/10.1063/1.5053989.
[41] Wohninsland A, Fetzer A-K, Riaz A, Kleebe H-J, Rödel J, Lalitha KV. Appl Phys Lett 2021;118:72903. https://doi.org/10.1063/5.0039369.
[42] Nagata H, Takagi Y, Yoneda Y, Takenaka T. APEX 2020;13:61002. https://doi.org/10.35848/1882-0786/ab8c1d.
[43] Li Z-T, Liu H, Thong H-C, Xu Z, Zhang M-H, Yin J, et al. Adv Electron Mater 2019;5:1800756. https://doi.org/10.1002/aelm.201800756.
[44] Lalitha KV. Materials 2021;14:2149. https://doi.org/10.3390/ma14092149.
[45] Jones JL. J Electroceram 2007;19:69–81. https://doi.org/10.1007/s10832-007-9048-z.
[46] Subbarao EC, Mcquarrie MC, Buessem WR. J Appl Phys 1957;28:1194–200. https://doi.org/10.1063/1.1722606.
[47] Daniels JE, Jo W, Rodel J, Jones JL. Appl Phys Lett 2009;95:32904. https://doi.org/10.1063/1.3182679.
[48] Hinterstein M, Schmitt LA, Hoelzel M, Jo W, Rodel J, Kleebe H-J, et al. Appl Phys Lett 2015;106:222904. https://doi.org/10.1063/1.4922145.
[49] Simons H, Daniels J, Jo W, Dittmer R, Studer A, Avdeev M, et al. Appl Phys Lett 2011;98:82901. https://doi.org/10.1063/1.3557049.
[50] Groszewicz PB, Breitzke H, Dittmer R, Sapper E, Jo W, Buntkowsky G, et al. Phys Rev B 2014;90:220104. https://doi.org/10.1103/PhysRevB.90.220104.
[51] Filik J, Ashton AW, Chang PCY, Chater PA, Day SJ, Drakopoulos M, et al. J Appl Crystallogr 2017;50:959–66. https://doi.org/10.1107/S1600576717004708.
[52] Pramanick A, Damjanovic D, Daniels JE, Nino JC, Jones JL. J Am Ceram Soc 2011;94:293–309. https://doi.org/10.1111/j.1551-2916.2010.04240.x.
[53] Weyland F, Acosta M, Vogler M, Ehara Y, Rodel J, Novak N. J Mater Sci 2018;53:9393–400. https://doi.org/10.1007/s10853-018-2232-5.
[54] Lalitha KV, Hinterstein M, Lee KY, Yang TN, Chen LQ, Groszewicz PB, et al. Phys Rev B 2020;101:174108. https://doi.org/10.1103/PhysRevB.101.174108.
[55] Jones JL, Hoffman M, Bowman KJ. J Appl Phys 2005;98:24115. https://doi.org/10.1063/1.1988978.
[56] Jones JL, Iverson BJ, Bowman KJ. J Am Ceram Soc 2007;90:2297–314. https://doi.org/10.1111/j.1551-2916.2007.01820.x.
[57] Jones JL, Slamovich EB, Bowman KJ. J Appl Phys 2005;97:34113. https://doi.org/10.1063/1.1849821.
[58] Hinterstein M, Lee KY, Esslinger S, Glaum J, Studer AJ, Hoffman M, et al. Phys Rev B 2019;99:174107. https://doi.org/10.1103/PhysRevB.99.174107.
[59] Oddershede J, Hossain MJ, Daniels JE. Appl Phys Lett 2016;109:92901. https://doi.org/10.1063/1.4961533.
[60] Daniels JE, Jo W, Rodel J, Honkimaki V, Jones JL. Acta Mater 2010;58:2103–11. https://doi.org/10.1016/j.actamat.2009.11.052.
[61] Ma C, Guo HZ, Beckman SP, Tan XL. Phys Rev Lett 2012;109:107602. https://doi.org/10.1103/PhysRevLett.109.107602.

Andreas Wohninsland is a PhD student in the research group Nonmetallic-Inorganic Materials of Prof. Jürgen Rödel at the Department of Materials Science, Technical University of Darmstadt, Germany. He received his BSc and MSc degrees in Geosciences from Heidelberg University in 2015 and 2018, respectively, focusing on experimental mineralogy. His research interests include synthesis and electrical and structural characterization of lead-free piezoceramics with the emphasis on X-ray diffraction techniques.

Dr. Lalitha Kodumudi Venkataraman (K.V. Lalitha) is currently a Group Leader at the Technical University of Darmstadt, Germany. She is the Principle Investigator of the Deutsche Forschungsgemeinschaft funded project on “Quenching enhanced lattice polarizability in lead-free ferroelectrics” (grant no. KO 5948/1-1, Nr. 414311761). She is also the recipient of the Alexander von Humboldt Postdoctoral Fellowship (2016–2018) and the Electroceramics 2020 Young Researcher Award. https://gepris.dfg.de/gepris/projekt/414311761?language=en, https://scholar.google.co.in/citations?hl=en&user=CY2OGgcAAAAJ&view_op=list_works&sortby=pubdate.